

Superconductivity up to 17 K in the high-pressure rhombohedral-I phase of ReO₃: a potential oxide analogy of hydride superconductors

P. F. Shan^{1,2#}, T. L. Lu^{1,2#}, Y. Y. Jiao^{1,3#}, Z. Y. Liu^{1,2#}, P. T. Yang^{1,2}, Y. Uwatoko⁴, X. L. Dong^{1,2}, B. S. Wang^{1,2}, J.-Q. Yan^{5*}, M. Liu^{1,2*}, J. P. Sun^{1,2*}, and J.-G. Cheng^{1,2*}

¹*Beijing National Laboratory for Condensed Matter Physics and Institute of Physics, Chinese Academy of Sciences, Beijing 100190, China*

²*School of Physical Sciences, University of Chinese Academy of Sciences, Beijing 100190, China*

³*Faculty of Science, Wuhan University of Science and Technology, Wuhan, Hubei 430065, China*

⁴*Institute for Solid State Physics, University of Tokyo, 5-1-5 Kashiwanoha, Kashiwa, Chiba 277-8581, Japan*

⁵*Materials Science and Technology Division, Oak Ridge National Laboratory, Oak Ridge, Tennessee 37831, USA*

These authors contributed equally to this work.

*E-mail: yanj@ornl.gov, mliu@iphy.ac.cn, jpsun@iphy.ac.cn, jgcheng@iphy.ac.cn

Abstract

As an *A*-site-vacant perovskite-type oxide, ReO₃ undergoes sequential pressure-driven structural transitions associated with the rotation of ReO₆ octahedra. The rhombohedral-I phase stable in the pressure range of 12-38 GPa is featured by a lattice of nearly close-packed oxygen layers intercalated with Re cations, in reminiscent of the recently discovered superhydride superconductors. A combined study of first-principles calculations and transport measurements under high pressures enabled us to discover superconductivity in the rhombohedral-I phase showing a dome-shaped $T_c(P)$ with a maximum T_c of 17 K at about 30 GPa. In addition to the enhanced density of states at the Fermi level compared to that of the ambient phase, the low-frequency vibrations of hexagonal-close-packed oxygen lattice significantly strengthen the electron-phonon coupling, which is responsible for observed superconductivity with a relatively high T_c . The present work thus establishes a rare case among oxide superconductors that the light-element oxygen lattice plays a crucial role in inducing superconductivity.

Keywords: ReO₃, structural transition, high pressure, superconductivity

ReO₃ is known as a purple-colored metallic oxide with high conductivity comparable to that of copper and silver [1]. It adopts an undistorted *A*-site-vacant perovskite-type structure consisting of corner-shared ReO₆ octahedra [2]. The covalent mixing between Re 5t_{2g} and O 2p_π orbitals through the linear Re-O-Re bonds is responsible for the excellent metallic conductivity [1,3]. It has been predicted to be a superconductor [4], but no superconductivity was observed experimentally down to 20 mK. In previous studies, the structural evolution of ReO₃ upon compression has attracted considerable attention because the absence of *A*-site cation in the cubic perovskite-type structure allows rigid rotation of the ReO₆ octahedra [5-8]. This leads to a sequence of pressure-driven structural transitions, *i.e.*, cubic-I (space group: *Pm*-3*m*) $\xrightarrow{0.5 \text{ GPa}}$ cubic-II (*Im* $\bar{3}$) $\xrightarrow{3 \text{ GPa}}$ monoclinic (*C2/c*) $\xrightarrow{12 \text{ GPa}}$ rhombohedral-I (*R* $\bar{3}c$) $\xrightarrow{38 \text{ GPa}}$ rhombohedral-II (*R* $\bar{3}c$), as illustrated in Fig. 1(a).

A close inspection on the structural features of these high-pressure (HP) variants revealed an interesting evolution of the oxygen lattice in the rhombohedral-I phase, which is stable in a wide pressure range of 12-38 GPa. As shown in Fig. 1(b), the rhombohedral-I phase can be derived from the cubic-I phase by a coupled rotation of ReO₆ octahedra around the <111> direction of the cubic structure [5]; this transforms the (111) plane of oxygen atoms from a kagome-type lattice in the cubic-I phase to a distorted triangular lattice in the rhombohedral-I phase. Assuming that the octahedron is rigid and the O-O distance within an octahedron is 2.65 Å, the rotation angle has been estimated to increase from 25° to 29° with increasing pressure from 12.8 to 34.5 GPa in the rhombohedral-I phase [5]. Meanwhile, the triangular oxygen lattice becomes more uniform, approaching hexagonal close packing at the rotation angle of 30°. Above 38 GPa, the rhombohedral-II phase with the same space group becomes stable; it has a twice longer *a*-axis and larger bulk modulus [5,6]. Since the oxygen atoms have already become close packed at ~ 38 GPa, the compression mechanism associated with the rotation of octahedra is no longer operational in the rhombohedral-II phase, where the octahedra must undergo compression to enable further reduction of the volume.

The close-packed oxygen layers cannot be realized in the cubic and monoclinic phases of ReO₃ or most other oxide materials. This makes the rhombohedral-I phase of ReO₃ a distinct case that can be described by a lattice of nearly close-packed oxygen layers intercalated with small Re atoms, as illustrated in Fig. 1(b). In light of the recent discovery of near-room-temperature superconductivity in the superhydrides [9,10], it is interesting to investigate how the light-element oxygen lattice would influence the phonon spectrum and the electrical transport properties of ReO₃ via modifying electron-phonon coupling. To this end, we are motivated to perform a combined study of first-principles calculations and transport measurements on ReO₃ under HP. This leads to a surprising discovery of superconductivity in the rhombohedral-I phase with an optimal

T_c of 17 K realized near the pressure where the closed-packed stacking of oxygen atoms is just formed around 30 GPa.

Theoretical calculations

The structural and electronic properties of ReO_3 were calculated by employing the DFT method at the GGA-PBE level at selected pressures. Details about the calculations are given in Supplemental Materials (SM). The crystal structure was fully relaxed from 0 to 34 GPa to mimic the structural phase evolutions of ReO_3 under external pressures. Our DFT calculations demonstrate that rotation of the ReO_6 octahedra in the cubic-I phase along the $\langle 111 \rangle$ axis densifies the oxygen layers and transforms it into the rhombohedral-I phase above 10 GPa, consistent with the experimental results. The ideal hexagonal close packing is realized at the rotation angle of 30° around 30 GPa. [Figure 2\(a-c\)](#) shows the calculated electronic density of state (DOS) at three representative pressures, *i.e.*, 0 GPa for the cubic-I structure, 15 and 30 GPa for the rhombohedral-I structure with different rotation angles. For all pressures, the Re-5*d* and O-2*p* orbitals are strongly hybridized and there is a considerable amount of contribution from the O-2*p* orbital to the DOS at Fermi level, $N(E_F)$. Importantly, the $N(E_F)$ increases with pressure, which changes slightly at 15 GPa but is almost doubled at 30 GPa in comparison with that at 0 GPa. Thus, the rhombohedral-I phase is theoretically predicted to possess enhanced $N(E_F)$ with strong hybridizations between Re-5*d* and O-2*p* orbitals.

In addition to $N(E_F)$, the contributions of oxygen lattice to the phonon spectrum and electron-phonon coupling (EPC) are also significantly enhanced with increasing pressure in the rhombohedral-I phase. [Fig. 2\(d-f\)](#) display the calculated phonon DOS (PhDOS), Eliashberg spectral function $\alpha^2F(\omega)$ and cumulative frequency-dependent EPC constant $\lambda(\omega)$ at three representative pressures. From the PhDOS, we can see that the lower frequency phonons ($< 250 \text{ cm}^{-1}$) are attributed to both Re and O, while the higher frequency phonons ($> 250 \text{ cm}^{-1}$) are dominated by the vibration modes of O. In addition, a gap opens around 250 cm^{-1} in the phonon spectrum of rhombohedral-I phase at 30 GPa. The most prominent features revealed in [Fig. 2\(d-f\)](#) are the significantly enhanced $\alpha^2F(\omega)$ and $\lambda(\omega)$ with increasing pressure in the rhombohedral-I phase. In particular, $\lambda(\omega)$ at 30 GPa in the frequency range $\sim 250\text{-}500 \text{ cm}^{-1}$ experiences an obvious upraise, which is primarily attributed to the phonon modes of the oxygen lattice mentioned above. The phonon dispersion curves at 30 GPa were presented in [Fig. 2\(g\)](#). The phonon linewidth calculations indicate that λ predominantly originates from the third, fourth, and fifth modes at the zone center Γ for the lower frequency phonons ($< 250 \text{ cm}^{-1}$). In contrast, the contributions to λ from the different phonon modes are comparable for the higher frequency phonons ($500\text{-}250 \text{ cm}^{-1}$). As shown in [Fig. 2\(h\)](#), the magnitude of EPC constant λ exhibits a fourfold enhancement from 0.2 at 0 GPa to

about 0.8 at 30 GPa, where the rotation angle approaches 30° in the rhombohedral-I phase. Such a large λ and enhanced $N(E_F)$ are favor of superconductivity.

Indeed, superconductivity is found theoretically throughout the rhombohedral-I phase based on the Eliashberg equation using the typical Coulomb pseudopotential and the calculated logarithmic average frequency of the phonon spectrum ω_{log} given in Fig. 2(h). As shown in Fig. 2(i), the superconducting T_c starts to emerge above 10 GPa, increases quickly with pressure, and finally reaches ~ 15 K at 34 GPa where the octahedral rotation angle approaches 30° in the rhombohedral-I phase.

Experimental verifications

To verify the above theoretical predictions, we carried out HP transport measurements on the ReO_3 single crystals using a BeCu-type diamond anvil cell (DAC). Details about the crystal growth and HP resistance measurements are given in SM. Figure 3 shows the $R(T)$ of ReO_3 single crystal (#2) under various pressures up to 65 GPa. The data were divided into three panels for (a) the cubic and monoclinic phases, (b) the rhombohedral-I, and (c) the rhombohedral-II phase, respectively. As seen in Fig. 3(a), $R(T)$ of the cubic and monoclinic phases show similar metallic behaviors without any anomaly. When increasing pressure to 10.7 GPa, the resistance at room temperature experiences an obvious increase and the $R(T)$ displays a broad hump centered around 150 K with some noticeable anomalies upon varying temperature, presumably due to the partial structural transformation to the rhombohedral-I phase. Interestingly, a clear drop of resistance appears at about 3.4 K, signaling the possible emergence of superconductivity as confirmed below.

As shown in Fig. 3(b), the resistance drop becomes steeper, moves to higher temperatures with increasing pressure, and eventually the resistance reaches zero at pressures over 12 GPa, thus confirming the occurrence of superconductivity in the rhombohedral-I phase. The evolution of the superconducting transition as a function of pressure can be visualized clearly from the plot of normalized $R(T)/R(20\text{ K})$ in Fig. 4(a). In addition to zero-resistance temperature, T_c^{zero} , here we also defined the onset T_c^{onset} , which reaches ~ 17.1 K at ~ 34 GPa. Upon further increasing pressure to above 40 GPa, as shown in Fig. 3(c), superconductivity is gradually suppressed in the rhombohedral-II phase and no sign of superconductivity can be discerned down to 1.5 K at pressures above 65 GPa. It is noted that $R(T)$ in the normal state experiences a monotonic enhancement with increasing pressure in the rhombohedral-I/II phases and evolves gradually into a nonmetallic behavior in the latter phase.

To further confirm and characterize the superconducting phase, we measured $R(T)$ under different magnetic fields at each pressure, Fig. S1. A presentative dataset recorded at 27.6 GPa is shown in Fig. 4(b), and all other data are given in the SM. As seen in Fig.

4(b), the superconducting transition is shifted gradually to lower temperatures with increasing field, and it remains quite sharp under 8 T. Here, we used the criteria of 50% R_n to define T_c and plotted the $\mu_0 H_{c2}(T)$ in Fig. 4(c). The slight upward curvature near zero field indicates the multi-band nature of the observed superconductivity in ReO_3 . Thus, we fit the $\mu_0 H_{c2}(T)$ by employing the following equation for a two-band superconductor in the dirty limit [11], *viz.*,

$$a_0[\ln t + U(D_1 h)][\ln t + U(D_2 h)] + a_2[\ln t + U(D_2 h)] + a_1[\ln t + U(D_1 h)] = 0 \quad (1)$$

Where $t = T/T_c$ is the reduced temperature, $h = \hbar\mu_0 H_{c2}/2\phi_0 k_B T$ is the dimensionless magnetic field with ϕ_0 the magnetic flux quantum, and D_n is the charge carriers diffusion coefficient. The coefficients a_0 - a_2 are defined as $a_0 = 2\omega/\lambda_0$, $a_1 = 1 + \lambda_-/\lambda_0$, $a_2 = 1 - \lambda_-/\lambda_0$ and $\lambda_- = \lambda_{11} - \lambda_{22}$, $\lambda_0 = \sqrt{\lambda_-^2 + 4\lambda_{12}\lambda_{21}}$, $\omega = \lambda_{11}\lambda_{22} - \lambda_{12}\lambda_{21}$ where λ is the superconducting coupling constants matrix. $U(x) = \psi(1/2 + x) - \psi(1/2)$, where $\psi(x)$ is the di-gamma function. As illustrated in Fig. 4(c), the experimental $\mu_0 H_{c2}(T)$ data at 27.6 GPa can be fitted excellently with the above two-band model, yielding a zero-temperature $\mu_0 H_{c2}(0) = 14.6$ T, which is smaller than the Pauli limit of $\mu_0 H_p^{\text{BCS}} = 1.84T_c = 28.3$ T. The $\mu_0 H_{c2}(T)$ data at other pressures are fitted and given in Fig. S2. The above analysis indicates that the observed superconductivity in the rhombohedral-I phase of ReO_3 should originate from multiple bands derived from the Re-5*d* and O-2*p* orbitals, consistent with the above DFT calculations.

The pressure dependence of $T_c(P)$ determined from different runs of $R(T)$ measurements was displayed in Fig. 5(a). It is clear that superconductivity emerges in the rhombohedral-I phase and develops into a broad superconducting $T_c(P)$ dome with an optimal $T_c \approx 17$ K near 30 GPa. It is noteworthy that the substantial enhancement of T_c follows nicely the rotation angle of ReO_6 octahedra and the highest T_c is achieved near the point where the close packing of the oxygen layer is just formed. Superconductivity is quickly suppressed in the rhombohedral-II phase. The presence of some pressure inhomogeneity might be responsible for the observed wide superconducting transition without a zero-resistance state. Different from the tendency of $T_c(P)$, $\mu_0 H_{c2}(P)$ shows a saturation behavior near the phase boundary between rhombohedral-I and -II, as shown in Fig. 5(b).

In coincidence with the emergence of superconductivity in the rhombohedral-I phase, the normal-state resistance experiences a sudden jump followed by a gradual enhancement upon further increasing pressure. This can be seen clearly from the pressure dependences of resistance at 280 and 20 K in Fig. 5(c), which defines the different structural variants with distinct transport properties. Thus, analyses of the normal-state transport properties would provide useful insights into the mechanism of superconductivity with relatively high T_c in the rhombohedral-I phase.

At ambient pressure, ReO_3 has been characterized as a simple metal with high carrier densities of $n_e \sim n_h = 4 \times 10^{21}/\text{cm}^2$ [12]. To track the evolutions of dominant charge carriers in different phases, we measured Hall resistance of ReO_3 single crystal (#3) at 20 K and different pressures with DAC in a van der Pauw configuration. All the $R_{xy}(H)$ data at 20 K are shown in Fig. S3 and the pressure dependence of carrier concentration $n = -(R_{\text{H}}e)^{-1}$ extracted from the Hall coefficient R_{H} are plotted in Fig. 5(d). Different from the ambient phase, the dominant charge carrier is altered to hole type in both the monoclinic and rhombohedral-I phases, and the carrier's concentration rises slightly across the transition to the latter phase. Then, the electron-type carriers become dominant in the rhombohedral-II phase. These results indicate that the electronic band structures undergo dramatic reconstruction accompanying the structural transitions in ReO_3 , and the hole-type charge carriers with enhanced density dominate the superconducting state of the rhombohedral-I phase.

The interaction between charge carriers with phonons is the key ingredient for superconductivity. To probe the lattice dynamics, we analyzed the normal-state resistance by the following equation[4,13], viz.

$$R(T) = R_0 + R_{\text{D}} \left(\frac{T}{\theta_{\text{D}}}\right)^5 \int_0^{\theta_{\text{D}}/T} \frac{z^5 dz}{(e^z - 1)(1 - e^{-z})} + R_{\text{E}} \left[\frac{T}{\theta_{\text{E}}} \sinh^2\left(\frac{\theta_{\text{E}}}{2T}\right)\right]^{-1} \quad (2)$$

where the first term R_0 is the residual resistance, and the second and third terms are the Bloch-Grüneisen and Einstein expressions, which represent the electron scattering by acoustic and optical phonons, respectively. R_{D} and R_{E} are resistance constant and θ_{D} and θ_{E} are Debye and Einstein temperatures, respectively. Both the $R(T)$ data of ReO_3 single crystals measured with DAC and the cubic anvil cell (CAC) can be well described by Eq. (2) and the obtained results are consistent with each other. The fitting results of CAC are shown in Fig. S4. As shown in Fig. 5(e), both θ_{D} and θ_{E} exhibit a dramatic drop when the monoclinic phase transforms to the rhombohedral-I phase at ~ 12 GPa. This indicates that the low-frequency ($< 500 \text{ cm}^{-1}$) phonon modes of oxygen in the rhombohedral-I phase play a crucial role for the observed superconductivity, consistent with the above first-principles calculations, Fig. 2(h).

The recognition of closed-packed oxygen lattice in the HP rhombohedral-I phase of ReO_3 enables us to discover superconductivity with a relatively high T_{c} via combined theoretical and experimental investigations. The optimal T_{c} of 17 K at ~ 30 GPa is higher than known rhenium-based oxides, including the superconducting $\text{Cd}_2\text{Re}_2\text{O}_7$ ($T_{\text{c}} \approx 1\text{-}2$ K) [14] with the pyrochlore structure and Hg_xReO_3 ($T_{\text{c}} \approx 7.7$ K@ 1atm and ≈ 11 K@ 4 GPa) [15] with the hexagonal bronze structure. To our knowledge, the optimal T_{c} is also the highest among the existing 5d transition-metal-based oxide superconductors. In sharp contrast to the aforementioned cases, the underlying mechanism for such a high T_{c} should be largely attributed to the low-frequency phonon modes from the oxygen

lattice, such as the optical phonon mode from breathing vibrations of oxygen coupled with the shocking modes of rhenium as shown in Fig. S5.

To quantify the contribution of light element to superconductivity, we made a rough comparison between the typical rare-earth superhydrides and ReO_3 . According to Ref. 10, for instance, in YH_9 and YH_{10} , the contribution of hydrogen to $N(E_F)$ is approximately 24% and 28%, while its contribution to λ is about 54% and 66%, respectively. In comparison, the corresponding contributions of oxygen to $N(E_F)$ and λ are 27% and $\sim 50\%$ in the present case of ReO_3 at 30 GPa. In this regard, the rhombohedral-I phase of ReO_3 can be considered as an oxide proxy to hydride superconductors that have aroused tremendous research interest recently.

In summary, the rhombohedral-I phase of ReO_3 was confirmed to be superconducting over a wide pressure range of 12-38 GPa, featured by a broad superconducting $T_c(P)$ dome with an optimal $T_c \approx 17$ K. In addition to the enhanced $N(E_F)$, the low-frequency phonon modes from the close-packed oxygen layers are found to play a crucial role in the observed superconductivity.

Acknowledgment. This work is supported by National Key R&D Program of China (2021YFA1400200), Beijing Natural Science Foundation (Z190008), National Natural Science Foundation of China (12025408, 11834016, 11921004, 11888101, 11904391, 12174424, 92065201), the Strategic Priority Research Program of CAS (XDB33000000), the CAS Project for Young Scientists in Basic Research, the CAS Interdisciplinary Innovation Team (JCTD-201-01), the Users with Excellence Program of Hefei Science Center CAS (2021HSC-UE008), and the Youth Innovation Promotion Association of CAS (2022YSBR-048, 2018010). Y. U. acknowledges the support from JSPS KAKENHI (JP19H00648). Work at ORNL was supported by the US Department of Energy, Office of Science, Basic Energy Sciences, Materials Sciences and Engineering Division. Part of the HP resistance measurements were performed at the CAC station of Synergic Extreme Condition User Facility (SECUF). HPXRD measurements were performed at the 4W2 HP station of the Beijing Synchrotron Radiation Facility (BSRF).

References

- [1] A. Ferretti, D. B. Rogers, and J. B. Goodenough, *J. Phys. Chem. Solids* **26**, 2007 (1965).
- [2] H. A. Evans, Y. Wu, R. Seshadri, and A. K. Cheetham, *Nat. Rev. Mater.* **5**, 196 (2020).
- [3] J. Falke, C. F. Chang, C. E. Liu, D. Takegami, A. Melendez-Sans, C. S. Chen, L. Zhao, A. C. Komarek, C. Y. Kuo, C. T. Chen, and L. H. Tjeng, *Phys. Rev. B* **103**, 115125 (2021).
- [4] P. B. Allen and W. W. Schulz, *Phys. Rev. B* **47**, 14434 (1993).

- [5] J.-E. Jorgensen, J. Staun Olsen, and L. Gerward, *J. Appl. Crystallogr.* **33**, 279 (2000).
- [6] E. Suzuki, Y. Kobayashi, S. Endo, and T. Kikegawa, *J. Phys. Condens. Matter.* **14**, 10589 (2002).
- [7] J.-E. Jorgensen, W. G. Marshall, R. I. Smith, J. Staun Olsen, and L. Gerward, *J. Appl. Crystallogr.* **37**, 857 (2004).
- [8] D. V. S. Muthu, P. Teredesai, S. Saha, Suchitra, U. V. Waghmare, A. K. Sood, and C. N. R. Rao, *Phys. Rev. B* **91**, 224308 (2015).
- [9] H. Liu, Naumov, II, R. Hoffmann, N. W. Ashcroft, and R. J. Hemley, *Proc. Natl. Acad. Sci. U. S. A.* **114**, 6990 (2017).
- [10] F. Peng, Y. Sun, C. J. Pickard, R. J. Needs, Q. Wu, and Y. Ma, *Phys. Rev. Lett.* **119**, 107001 (2017).
- [11] A. Gurevich, *Phys. Rev. B* **67**, 184515 (2003).
- [12] Q. Chen, Z. Lou, S. Zhang, Y. Zhou, B. Xu, H. Chen, S. Chen, J. Du, H. Wang, J. Yang, Q. Wu, O. V. Yazyev, and M. Fang, *Phys. Rev. B* **104**, 115104 (2021).
- [13] T. Tanaka, T. Akahane, E. Bannai, S. Kawai, N. Tsuda, and Y. Ishizawa, *J. Phys. C: Solid State Phys.* **9**, 1235 (1976).
- [14] M. Hanawa, Y. Muraoka, T. Tayama, T. Sakakibara, J. Yamaura, and Z. Hiroi, *Phys. Rev. Lett.* **87**, 187001 (2001).
- [15] K. Ohgushi, A. Yamamoto, Y. Kiuchi, C. Ganguli, K. Matsubayashi, Y. Uwatoko, and H. Takagi, *Phys. Rev. Lett.* **106**, 017001 (2011).

Figures and captions

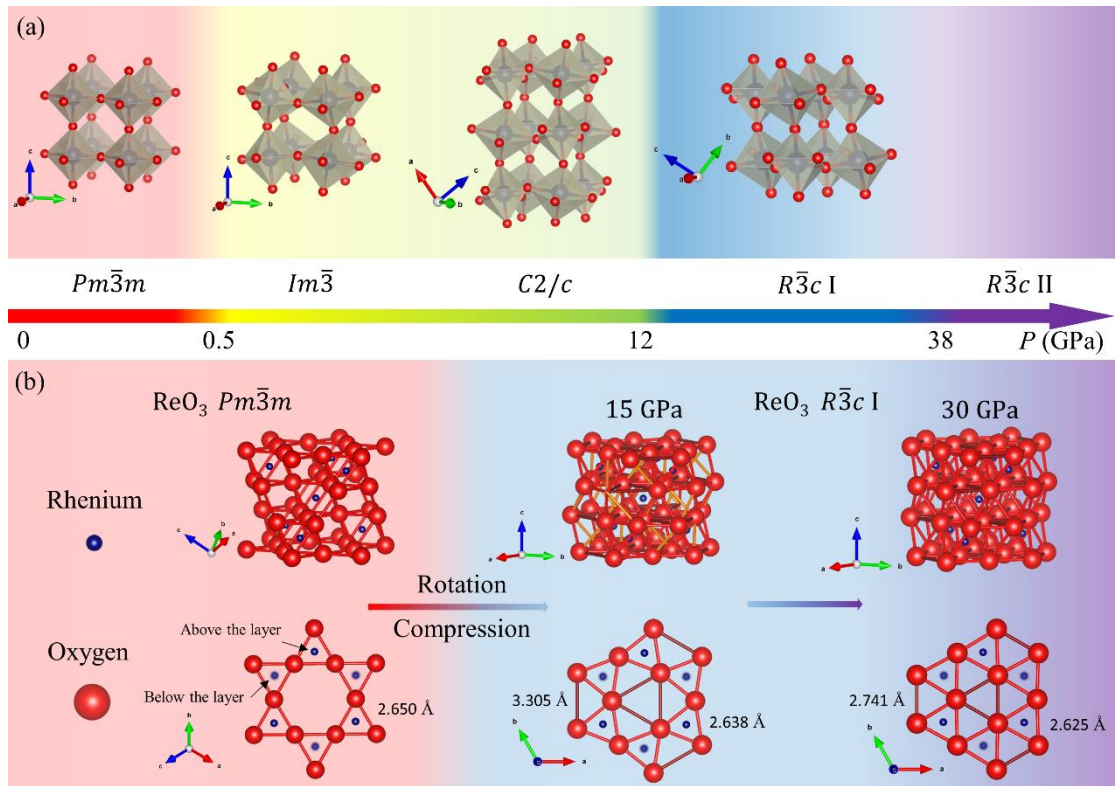


Fig. 1. (a) The structure evolutions of ReO_3 under high pressure, the color bar shows the different structural phases of ReO_3 and their pressure ranges. (b) The view of the oxygen lattice and layers of ReO_3 , the top shows the rotation of octahedra from $Pm\bar{3}m$ to $R\bar{3}c$ I, and the bottom shows the oxygen layers.

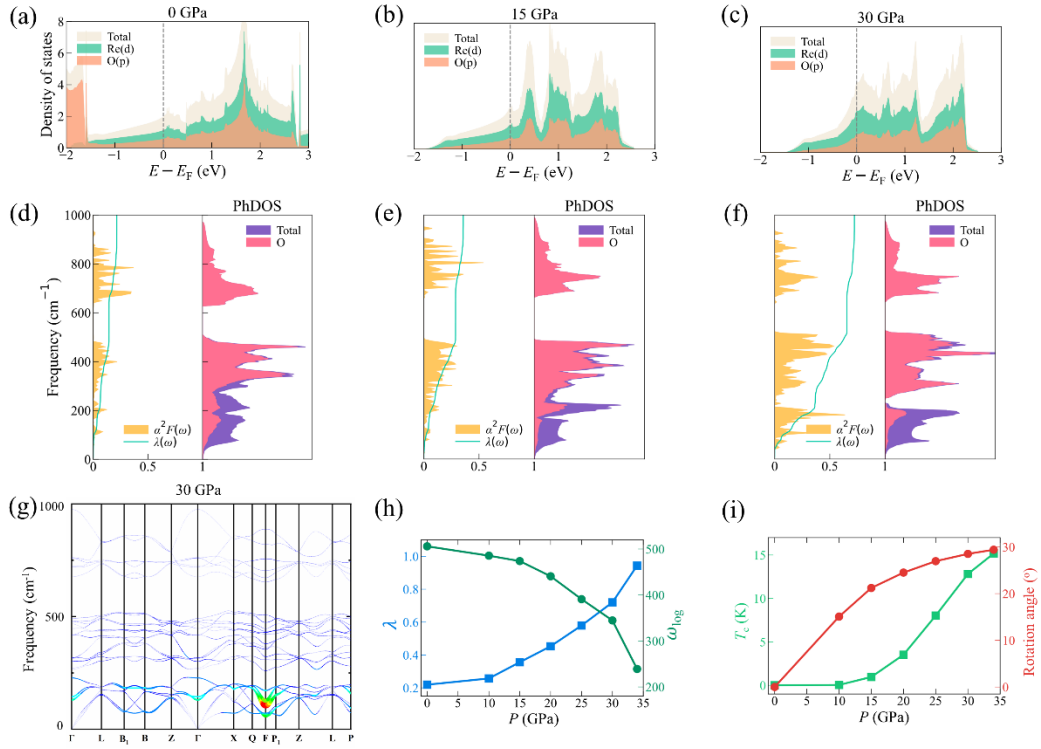


Fig. 2. Total density of states (DOS) and partial DOS for ReO₃ at (a) 0, (b) 15, and (c) 30 GPa. The energy zero represents the Fermi level. Eliashberg spectral function $\alpha^2 F(\omega)$, and cumulative frequency-dependent electron-phonon coupling (EPC) constant $\lambda(\omega)$, total phononic density of states (PhDOS) and partial PhDOS at (d) 0, (e) 15, and (f) 30 GPa. (g) Phonon dispersion curves at 30 GPa. The linewidth indicates the strength. (h) Calculated λ , ω_{log} , (i) T_c , and rotation angle as a function of pressure.

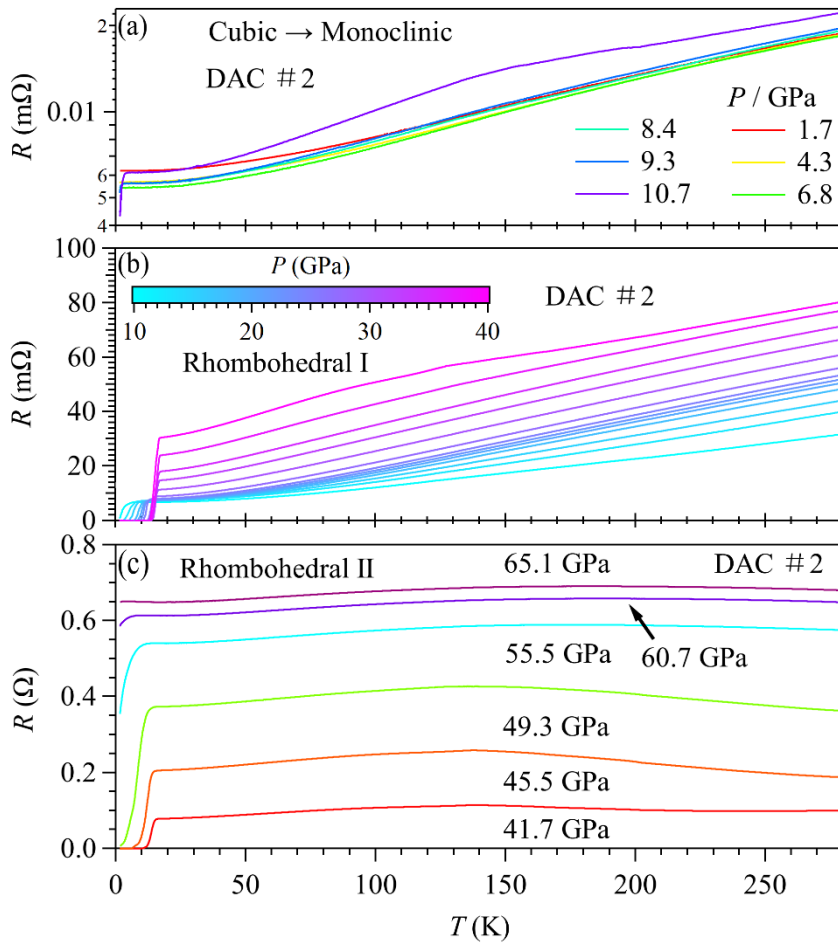


Fig. 3. Temperature-dependent resistance of ReO_3 (DAC #2) at various pressures (a) from 1.7 to 10.7 GPa for the cubic and monoclinic phases, (b) from 12.0 to 37 GPa in the rhombohedral-I phase, and (c) from 41.7 GPa to 65.1 GPa in the rhombohedral-II phase.

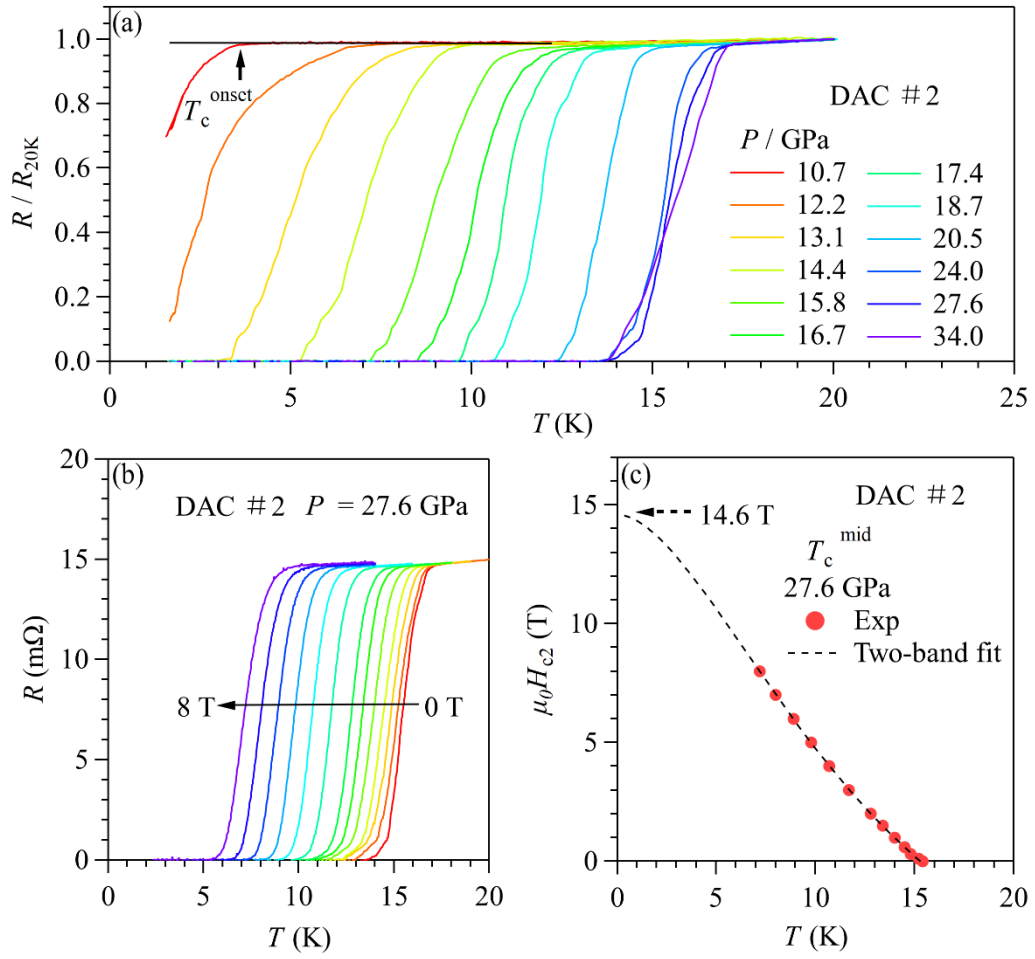


Fig. 4. (a) Normalized resistance R/R_{20K} of ReO₃ (DAC #2) under different pressures. (b) Temperature dependences of resistance under various magnetic fields at 27.6 GPa. (c) Temperature dependence of $\mu_0 H_{c2}(T)$ at 27.6 GPa fitted by WHH two-band model, Eq. (1) in the main text.

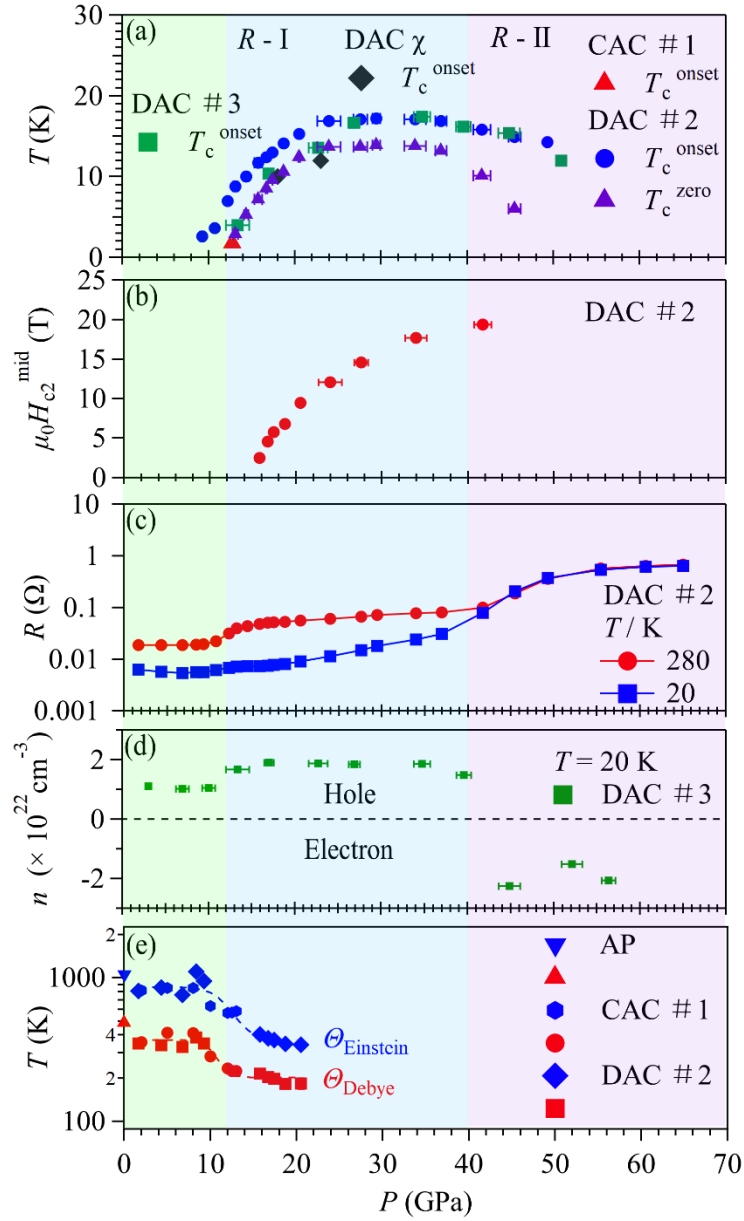


Fig. 5. Pressure dependences of (a) the superconducting transition temperature in different runs, (b) the upper critical field $\mu_0 H_{c2}(0)$, (c) the resistance at 20 and 280 K, (d) the carrier concentration at 20 K, (e) the estimated Debye and Einstein temperatures.